Solid Earth Discuss., 5, 1771–1815, 2013
www.solid-earth-discuss.net/5/1771/2013/
doi:10.5194/sed-5-1771-2013

Solid Earth
Discussions
Open Access

Testing the effects of the numerical implementation of water migration on models of subduction dynamics

M. E. T. Quinquis[1] **and S. J. H. Buiter**[1,2]

[1]Geodynamics Team, Geological Survey of Norway (NGU), Trondheim, Norway
[2]Centre for Earth Evolution and Dynamics, University of Oslo, Oslo, Norway

Received: 23 September 2013 – Accepted: 27 September 2013 – Published: 24 October 2013

Correspondence to: M. E. T. Quinquis (matthieu@quinquis.net)

Published by Copernicus Publications on behalf of the European Geosciences Union.

Abstract

Subduction of oceanic lithosphere brings water into Earth's upper mantle. Previous numerical studies have shown how slab dehydration and mantle hydration can impact the dynamics of a subduction system by allowing a more vigorous mantle flow and promoting localisation of deformation in lithosphere and mantle. The depths at which dehydration reactions occur in the hydrated portions of the slab are well constrained in these models by thermodynamic calculations. However, the mechanism by which free water migrates in the mantle is incompletely known. Therefore, models use different numerical schemes to model the migration of free water. We aim to show the influence of the numerical scheme of free water migration on the dynamics of the upper mantle and more specifically the mantle wedge. We investigate the following three migration schemes with a finite-element model: (1) element-wise vertical migration of free water, occurring independent of the material flow; (2) an imposed vertical free water velocity; and (3) a Darcy velocity, where the free water velocity is calculated as a function of the pressure gradient between water and the surrounding rocks. In addition, the material flow field also moves the free water in the imposed vertical velocity and Darcy schemes. We first test the influence of the water migration scheme using a simple Stokes flow model that simulates the sinking of a cold hydrated cylinder into a hot dry mantle. We find that the free water migration scheme has only a limited impact on the water distribution after 1 Myr in these models. We next investigate slab dehydration and mantle hydration with a thermomechanical subduction model that includes brittle behaviour and viscous water-dependent creep flow laws. Our models show how the bound water distribution is not greatly influenced by the water migration scheme whereas the free water distribution is. We find that a water-dependent creep flow law results in a broader area of hydration in the mantle wedge which feeds back to the dynamics of the system by the associated weakening. This supports using dynamic time evolution models to investigate the effects of (de)hydration. We also show that hydrated material can be transported down to the base of the upper mantle at 670 km. Although (de)hydration

processes influence subduction dynamics, we find that the exact numerical implementation of free water migration is not important. This implies that a simple implementation of water migration would be sufficient for studies that focus on larger-scale features of subduction dynamics.

1 Introduction

Dehydration of subducting lithosphere and the related hydration of the mantle wedge can influence the dynamics of subduction, as water has a weakening effect on viscous and brittle rheologies (e.g., Sibson et al., 1975; Peacock, 1987; Hirschmann, 2006; Connolly, 2005; Gerya et al., 2007). The amount of fluids carried by subducting oceanic lithosphere is debated, but it is thought that water content can reach up to 3 wt.% at the surface, decreasing with depth (Rüpke et al., 2004). Water is acquired through near-surface hydration, which is aided by flexure-related extensional fractures, and by hydrothermal activity with circulation of hot water and vapour in the upper section of the crust (Staudigel, 2003; Rüpke et al., 2004; Faccenda et al., 2008).

The subducting crust carries water in two phases: (1) free fluids, contained either in the porosity of the rock (Stern, 2002; Bercovici and Karato, 2003; Rüpke et al., 2004) or percolating along the grain boundaries (Wark et al., 2003; Cheadle et al., 2004), and (2) mineralogically bound fluids in the form of a hydroxyl complex (OH) (Schmidt and Poli, 1998; Hirschmann, 2006). Once a slab starts to subduct, it undergoes dehydration processes due to the increase in pressure and temperature. Most of the water contained in the porosity of the rock is expelled at the trench through compaction and is not transported into the mantle (Stern, 2002; Rüpke et al., 2004). Hydrated minerals include, among others, amphiboles, chlorite and serpentine. It has been well documented that mineralogically bound water is released when phase transitions occur (Schmidt and Poli, 1998; Iwamori, 1998; Kerrick and Connolly, 2001; Ohtani et al., 2004; Rüpke et al., 2004; Syracus and Abers, 2006; Hirschmann, 2006). At the same time, experimentally determined phase diagrams suggest that mineralogically bound water can be trans-

SED
5, 1771–1815, 2013

ported to the base of the upper mantle, or perhaps even grater depths (Iwamori, 1998; Schmidt and Poli, 1998; Stern, 2002; Ohtani et al., 2004).

Dehydration processes can influence subduction in multiple ways. For example, the depth at which major dehydration occurs determines the location of volcanic arcs, which are located ca. 110–120 km above the surface of subducted slabs (England et al., 2004; Syracus and Abers, 2006). It is the melting of mantle wedge materials that is thought to lead to arc volcanism. But water released from the subducting slab decreases the pressure and temperature at which melting occurs, thus enhancing mantle wedge melting and causing volcanism. Water released by slab dehydration can form cold wet plumes that efficiently hydrate the mantle wedge (Billen and Gurnis, 2001; Billen, 2008; Gorczyk et al., 2007; Richard and Iwamori, 2010). These fluids can then cause a more vigorous flow in the mantle wedge. Arcay et al. (2005) showed that mantle wedge hydration can result in thermal erosion and softening of the overriding lithosphere. Water is also thought to help subduction initiation by promoting failure of the lithosphere in a narrow shear zone under sediment loading (Regenauer-Lieb et al., 2001). Once subduction has started, (de)hydration processes may further influence the evolution of subduction by enforcing an asymmetrical geometry of subduction zones, causing subduction to be one-sided (Gerya et al., 2007). Dehydration processes can in addition aid the exhumation of high and ultrahigh-pressure metamorphic rocks by creating a wide and weak subduction channel through which rocks are exhumed (Gerya et al., 2002). Dehydration of the subducting slab must increase slab strength, but this effect may be overwhelmed by the strong impact of water on the mantle wedge.

The models mentioned above use similar methods to determine the conditions of pressure and temperature at which dehydration processes occur. These are usually based on thermodynamic calculations (de Capitani and Brown, 1987; Holland and Powell, 1998; Powell et al., 1998; Connolly, 2005) or high pressure experiments (Schmidt and Poli, 1998; Ohtani et al., 2004; Komabayashi et al., 2005; Iwamori, 2007), and the location of the dehydration fronts during subduction do not greatly vary between models. However, exactly how water migrates in the lithosphere and the mantle is not well

SED
5, 1771–1815, 2013

M. E. T. Quinquis and S. J. H. Buiter

constrained. Bound water migrates with the material flow while free water can migrate in the interconnected porosity of the crust and sediments (Stern, 2002; Rüpke et al., 2004), percolate along grain boundaries in the mantle (Wark et al., 2003; Cheadle et al., 2004), create its own hydrated channels (Katz et al., 2006), or be absorbed by non-saturated rocks of the mantle wedge (Iwamori, 1998) to be potentially transported with the mantle flow into the lower mantle (Bercovici and Karato, 2003; Iwamori, 2007; Richard and Bercovici, 2009; Fujita and Ogawa, 2013). Water migration paths are influenced by the flow in the mantle wedge and this can result in cases where part of the free water migrates up through the mantle wedge, while the rest is subducted into the mantle (Cagnioncle et al., 2007).

Numerical studies of hydration of the mantle have used different numerical approximations for the migration of free water in the mantle:

1. Free water migrates vertically in the upper mantle and is not coupled to material flow in the mantle wedge (Arcay et al., 2005; Richard et al., 2006, 2007; Richard and Iwamori, 2010).

2. The migration of free water is vertical, but coupled to the mantle flow. The effective migration path of water is therefore no longer purely vertical, but can include a horizontal component. This method has been implemented as an imposed vertical velocity added to the velocity of the material flow (Gorczyk et al., 2007) or as a dehydration front (Gerya et al., 2002) with an imposed horizontal and vertical velocity.

3. Free water migrates as a Darcy flow, following the mean stress or pressure gradient in the mantle wedge (Cagnioncle et al., 2007). Darcy flow changes the migration paths of fluids which are now no longer necessarily vertical (Cagnioncle et al., 2007). Also here the material flow may displace free water in addition to the Darcy mechanism.

These different water migration schemes do show differences in the spatial distribution of water as the subduction system evolves. As discussed above, several studies have

SED
5, 1771–1815, 2013

M. E. T. Quinquis and S. J. H. Buiter

numerically investigated the effects of slab dehydration and mantle wedge hydration on subduction processes. However, the influence of the numerical implementation of water migration on subduction model dynamics has not been investigated until now.

We aim to investigate the role of different numerical water migration schemes on the dynamics of the subducting slab and the mantle wedge. We keep our models simple, allowing us to focus on the first order effects of dehydration and water migration. Our models do therefore not include melting, shear heating, or adiabatic heating. We first illustrate the effects of dehydration and water migration for a simple model of a cold and hydrated cylinder sinking in a warm mantle. Our second series of models examines the effects of (de)hydration and water migration on a thermo-mechanical subduction model at the scale of the upper mantle.

2 Modelling approach

2.1 Equations for thermo-mechanical slow flows

We solve the equations for conservation of mass (assuming incompressibility) (Eq. 1), momentum (Eq. 2) and energy (Eq. 3):

$$\nabla \cdot \boldsymbol{v} = 0 \tag{1}$$

$$-\nabla P + \nabla \cdot \bar{\sigma}' + \rho \boldsymbol{g} = 0 \tag{2}$$

$$\rho C_p \frac{\partial T}{\partial t} = k \nabla^2 T - \rho C_p \boldsymbol{v} \cdot \nabla T + H \tag{3}$$

$\boldsymbol{v}$ is the velocity vector, ρ density, t time, P pressure (mean stress), $\bar{\sigma}'$ deviatoric stress tensor, $\boldsymbol{g}$ gravitational acceleration ($g_x = 0$ and $g_y = -9.81\,\mathrm{m\,s^{-2}}$), C_p specific heat, T temperature, k thermal conductivity, and H radioactive heat production per unit volume. In the subduction models, the Boussinesq approximation is assumed i.e., $\frac{\partial \rho}{\partial t} = 0$ but $\rho = \rho_0(1 - \alpha(T - T_0))$ where ρ_0 is the reference density at $T = T_0$ and α is the volumetric thermal expansion coefficient.

SED
5, 1771–1815, 2013

M. E. T. Quinquis and S. J. H. Buiter

Materials deform either viscous or brittle. Our viscous rheologies are linear or pressure- and temperature-dependent:

$$\eta_{\mathrm{df,ds}} = \frac{1}{2}\left(\frac{d^p}{A\ C_{\mathrm{OH}}^r}\right)^{\frac{1}{n}}\ \dot{\varepsilon}_{\mathrm{e}}'^{\ \frac{1-n}{n}}\ e^{\left(\frac{Q+PV}{nRT}\right)} \tag{4}$$

$\dot{\varepsilon}_{\mathrm{e}}'$ is the effective deviatoric strain rate ($\dot{\varepsilon}_{\mathrm{e}}' = (\frac{1}{2}\dot{\varepsilon}_{ij}'\dot{\varepsilon}_{ij}')^{\frac{1}{2}}$), A is a material constant, n is the power law stress exponent, d grain size, p grain size exponent, C_{OH} water content, r water content exponent, Q activation energy, V activation volume and R molar gas constant. df and ds refer, respectively, to deformation by diffusion creep ($p > 0$ and $n = 1$) and dislocation creep ($p = 0$ and $n > 1$). Diffusion and dislocation creep are assumed to act in parallel in all materials, resulting in a composite viscosity (η_{comp}) (Karato and Li, 1992; van den Berg et al., 1993):

$$\eta_{\mathrm{comp}} = \left(\frac{1}{\eta_{\mathrm{ds}}} + \frac{1}{\eta_{\mathrm{df}}}\right)^{-1} \tag{5}$$

In our models only bound water influences the viscosity and we only consider the impact of water on sub-crustal materials. A water content of 4000 ppm results in a viscosity decrease by ca. 2 orders of magnitude when using the dislocation or diffusion creep flow law for wet olivine from Hirth and Kohlstedt (2003). This can result in viscosities that are lower than the minimum viscosity of 10^{18} Pa s which is imposed in our models. We, therefore, assume that materials are fully hydrated and C_{OH} no longer varies once water content exceeds 4000 ppm.

Brittle behaviour in the subduction models follows a Druker–Prager criterion (Handin, 1969; Jaeger and Cook, 1976; Twiss and Moores, 1992):

$$\sigma_{\mathrm{e}}' = P\sin\phi + C\cos\phi \tag{6}$$

σ_{e}' is the effective deviatoric stress ($\sigma_{\mathrm{e}}' = (\frac{1}{2}\sigma_{ij}'\sigma_{ij}')^{\frac{1}{2}}$), ϕ is the angle of internal friction, and C is the cohesion. ϕ undergoes a linear decrease with total effective strain (measured as the second invariant of the strain tensor) to simulate strain-weakening. Such

SED
5, 1771–1815, 2013

M. E. T. Quinquis and S. J. H. Buiter

strain weakening is thought to result from a reduction in fault rock grain size (Handy et al., 2007), mineral transformations (White and Knipe, 1978; Tingle et al., 1993), or the development of foliation or high fluid pressures (Hubbert and Rubey, 1959; Sibson, 1977). The effective viscosity for plastic flow is (Lemiale et al., 2008):

$$\eta_p = \frac{P\sin\phi + C\cos\phi}{2\dot{\varepsilon}'_{\mathrm{e}}} \tag{7}$$

In our thermo-mechanical subduction models, we use a minimum viscosity value of 10^{18} Pa s and a maximum cut-off of 10^{24} Pa s. These values ensure efficient convergence of our mechanical solution, while allowing for viscosity contrasts of 6 orders of magnitude. We solve the thermal and mechanical equations with a 2-D version of SULEC, which is an Arbitrary Lagrangian Eulerian (ALE) finite element code (Buiter and Ellis, 2012). The mesh consists of quadrilateral elements which have linear continuous velocity and constant discontinuous pressure fields. Materials are tracked with particles. We use harmonic viscosity averaging and arithmetic density averaging schemes from particles to elements (Schmeling et al., 2008). The subduction models have a free surface and we use the surface stabilisation algorithm of Kaus et al. (2010) and Quinquis et al. (2011).

2.2 Calculation of water content

Our subduction model includes 3 lithologies: a Bulk Oceanic Crust (BOC), Serpentinised Harzburgite (SHB) for the lithospheric mantle (Chemia et al., 2010), and Pyrolite for the sub-SHB mantle (Schmidt and Poli, 1998). Water content is determined in wt.% as a function of pressure, temperature and bulk composition (i.e., the average chemical composition of each lithology, Table 1). The water contents of BOC and SHB are calculated using Perple_X (Connolly, 2005) by Chemia et al. (2010) (Fig. 1). Perple_X is a thermodynamic code that minimises the Gibbs free energy of a chemical system to determine the stability fields of the phases which compose the mineral assemblages.

SED
5, 1771–1815, 2013

M. E. T. Quinquis and S. J. H. Buiter

Once these stability fields are calculated, it is possible to determine the maximum allowed water content of each phase as a function of pressure and temperature. The thermodynamic calculations of Perple_X are valid up to pressures of 7 GPa and temperatures of 1300 °C and do therefore not cover upper mantle conditions. We base our water contents in the upper mantle on Schmidt and Poli (1998) who experimentally determined maximum water content for pyrolite up to 8 GPa and 1100 °C. We extrapolate these data to 11 GPa and 1400 °C by linearly continuing the Clapeyron slopes of the stability fields, similar to Arcay et al. (2005) (Fig. 2). Serpentinisation of the mantle wedge can locally increase the maximum water content up to 7 wt.% H_2O (Iwamori, 1998; Rüpke et al., 2004; Connolly, 2005). We furthermore assume that the maximum water content in the sublithospheric mantle (i.e., the pyrolitic material) does not become less than 0.2 wt.%, following Bercovici and Karato (2003) (Fig. 2). Multiplying wt.% of water with 10^4 gives ppm of water which is used in the flow laws (Eq. 4).

2.3 Water migration schemes

In our models, mineralogically bound water is advected with the material flow. Each particle therefore carries not only a material identifier, but also its bound water value. Free water migrates following one of these imposed migration schemes: (1) elemental and vertical; (2) imposed vertical velocity; or (3) Darcy flow velocity. All water migration schemes follow three stages: (1) determine the maximum allowed water content of each particle and the amounts of free and bound water, (2) move the free water, if present, and (3) distribute the free water along the migration path. For every particle we calculate the maximum bound water that the particle can contain using a standard bilinear interpolation in pressure and temperature of wt.% H_2O on gridded versions of Figs. 1 and 2. If the mineralogically bound water is less than the maximum water content, the particle is undersaturated and no free water is produced. If the mineralogically bound water of the particle exceeds the maximum water content, it is oversaturated in water and dehydration occurs. The amount of free water is the difference between the

SED
5, 1771–1815, 2013

M. E. T. Quinquis and S. J. H. Buiter

mineralogical bound water of the particle and the maximum allowed water. The free water migrates through the model following one of the schemes we are investigating.

The first migration scheme assumes that free water moves vertically upwards owing to its negative buoyancy, with one element per time step (Δt) and is not affected by the material flow in the model (Arcay et al., 2005). This implies that the water migration velocity is purely vertical and is imposed as the local vertical grid size divided by the time step. A model using a variable grid size would not have a constant free water velocity and this should therefore be avoided. If free water is present, undersaturated particles in the current element are hydrated first. If free water remains after this first step, it migrates to the element above. There it hydrates the undersaturated particles of that element from the bottom up. If all particles are saturated and free water is still present, it is evenly distributed over all particles of the element, waiting for the next time step for further upward migration.

The second migration scheme imposes the velocity for free water ($v_{f,x}$ and $v_{f,y}$) (Richard et al., 2006; Gorczyk et al., 2007; Faccenda et al., 2008). This method reduces the grid dependence of the migration scheme, though does not necessarily eliminate it totally. When a particle is oversaturated, it releases water distributed along the path defined by $v_f \times \Delta t$ (Fig. 3). The horizontal and vertical components of the material flow are added to the respective components of the free water velocity. Migration of free water is therefore no longer necessarily vertical. As in the case of the elemental migration scheme, the first step is to hydrate undersaturated particles in the current element. If free water is still present after this step, the remaining free water migrates to the next element, saturating the undersaturated particles from the bottom up, and so on. If all particles along the migration path of this time step are saturated (i.e., all particles in elements 1 to 6 of Fig. 3), the remanding water is distributed evenly over all particles of the last element. The motivation for element-wise distribution is that water migration paths are likely irregular and a linear path for free water would be unlikely (Rüpke et al., 2004; Katz et al., 2006). We only show examples with an imposed vertical velocity and $v_{f,x} = 0$.

SED
5, 1771–1815, 2013

The third migration scheme follows the pressure gradient caused by the difference in density between the fluid and the solid it is percolating through. We neglect the dynamic component of the pressure gradient which could be caused by the solid flow, because in our subduction models pressures are mainly lithostatic. This migration scheme is characterised by the Darcy velocity:

$$v_{\mathrm{f},y} = \varpi \times \frac{(\rho_\mathrm{s} - \rho_\mathrm{f}) g\, d^2\, \Phi^2}{270\, \eta_\mathrm{f}} \tag{8}$$

where $v_{\mathrm{f},y}$ is the vertical fluid velocity, ϖ an efficiency factor, ρ_s and ρ_f the density of the solid and fluid respectively, g the gravitational acceleration, Φ the volume fraction of fluid, d the grain size (same as in Eq. 4), and η_f the viscosity of the fluid. The water migration and distribution then follow scheme 2. Φ, the volume fraction of fluid, is determined from the initial water content and the grids for pressure, temperature and wt.% H_2O. However, this assumes that all the free water is present in interconnected channels which would result in unnaturally high fluid velocities. We therefore introduce an efficiency factor, ϖ, that corresponds to the percentage of interconnected channels of the network through which water can migrate. This reduces the effective fluid velocity because water can only migrate through the interconnected network. The Darcy water velocity is calculated for every particle of the model. The water velocity is not constant throughout the model and areas with higher water content have higher water migration velocities. Free water is again also moved by the material flow field in addition to the Darcy velocity.

We use the following output values to quantify the influence of the water migration schemes on the water distribution and the dynamic evolution of the models: (1) the water distribution is described by tracking the depths of the top-most and lower-most particles of hydrated material. The top hydrated particle gives insight into the effective water migration velocity, which is not necessarily the same as the imposed water migration velocity. For example, assuming a high water migration velocity and a low amount of free water, free water will first saturate undersaturated materials resulting in an ef-

SED
5, 1771–1815, 2013

M. E. T. Quinquis and S. J. H. Buiter

Title Page
Abstract | Introduction
Conclusions | References
Tables | Figures
◀| |▶
◀ ▶
Back | Close
Full Screen / Esc
Printer-friendly Version
Interactive Discussion

fectively lower velocity of the hydration front. (2) The root-mean-square water contents for slab or cylinder and the mantle provide information on the rate of dehydration of the slab or cylinder and the mantle. (3) For Stokes flow models in which viscosity depends on water content, the bottom-most particle of the subducting cylinder is also tracked. This shows the influence of water content on the dynamic evolution of the model.

3 The effects of (de)hydration on simple Stokes flow

3.1 Stokes model setup

We first investigate the effects of (de)hydration and water migration with a simple model which simulates the subduction of a detached piece of lithosphere by the sinking of a cold, hydrated cylinder into a warm, dry mantle. These experiments are based on simple Stokes flow and use linear viscous rheologies. We solve for the advection and conduction of temperature in addition to the mechanical flow, but do not couple the thermal and mechanical aspects of the models.

The model domain is 300 km × 300 km and has a uniform Eulerian resolution of 1 km × 1 km elements. The initial particle density is 25 particles per element. In this series of experiments no particle injection or deletion scheme is used. The cold cylinder has a radius of 20 km and is centered on the coordinates $x = 150$ km $y = -130$ km (Fig. 4). A strong viscosity contrast between the cylinder and the mantle avoids deformation of the cylinder (Table 2). The mechanical boundary conditions are free-slip on all sides (i.e., the velocity component parallel to the boundary is free, whereas the velocity component perpendicular to the boundary is zero). A 20 Myr old lithosphere, 58 km thick, overlies the mantle. The initial thermal condition of the oceanic lithosphere is determined from the plate cooling model (e.g., Turcotte and Schubert, 2002) for a surface temperature of 0 °C, a temperature of 1300 °C at 58 km, and a thermal diffusivity of 10^{-6} m^2 s^{-1}. The surface temperature is held at 0 °C and the bottom temperature (at $y = -300$ km) at 1360.5 °C throughout model evolution, while the lateral sides are insu-

SED
5, 1771–1815, 2013

lated (zero heat flux). A high conductivity ($k = 105\,\mathrm{W\,m^{-1}\,K^{-1}}$) is used in the mantle to enforce a mantle adiabat of $0.25\,^{\circ}\mathrm{C\,km^{-1}}$ (Pysklywec and Beaumont, 2004). The initial temperature of the cylinder is 400 °C which gradually increases as the cylinder warms up. The mantle is of pyrolitic composition, while the lithosphere and the cylinder are composed of SHB. The material and thermal properties are in Table 2. The initial water content of the hydrated cylinder is imposed at 2000 ppm.

This model setup is run using the three different migration schemes (see Sect. 2.3). First, we use an elemental vertical migration of free water. The water migration velocity is the vertical element size divided by the time step: $20\,\mathrm{cm\,yr^{-1}}$. Second, we use the vectorial migration scheme, imposing a vertical free water velocity of 10, 20 and $60\,\mathrm{cm\,yr^{-1}}$. As we use a uniform grid resolution, the $20\,\mathrm{cm\,yr^{-1}}$ model should be similar to the elemental scheme. However, the schemes are not identical because the vertical imposed velocity scheme assumes that free water is also displaced by the material flow field. Finally, we use the vectorial migration scheme where the vertical water velocity is calculated from the Darcy equation (Eq. 8).

3.2 Stokes model results

We first examine models in which water content does not influence the linear viscosity. The thermal and mechanical evolution of these models are therefore identical. These models are used to test cylinder dehydration and mantle hydration for the three free water migration schemes.

As only the water migration schemes are changed, the evolution of the cylinders dehydration is identical in all cases. Dehydration of the cylinder occurs due to the increase in temperature of the cylinder from the outer rim inwards (Fig. 5a). Dehydration processes are assumed to be nearly instantaneous, whereas water migration velocities are more than an order of magnitude larger than the flow velocities of the mantle. Therefore, the influence of pressure on dehydration is negligible as the cylinder does not sink as quickly as it dehydrates. The hydrated cylinder is initially undersaturated as

SED
5, 1771–1815, 2013

the initial water content is 0.2 wt.% (but it could contain up to 6.8 wt.% at its initial pressure and temperature). The interior of the cylinder is therefore hydrated by water from the lower rim, which undergoes dehydration. This explains the differences observed in cylinder OH_{rms} during the first 1 Myr of model evolution (Fig. 6). Once the centre of the subducting cylinder becomes saturated, dehydration in all models converges (Fig. 6c, f, i).

Hydration of the mantle initiates at the lateral sides of the cylinder, as the interior is being hydrated (Fig. 5b). This results in a horned-shape area of hydrated mantle, which progresses inwards as the cylinder dehydrates. The spatial distribution of bound water is affected by the flow of the mantle. This is visible in the area of hydrated mantle above the cylinder: a minimum in width of the hydrated domain occurs at a depth of ca. 125 km (Fig. 5a, last stage). This thinning is accentuated as the cylinder sinks towards the bottom of the model domain. The spatial distribution of free water is not affected by the mantle flow as water migration velocities are much higher than the mantle flow velocities.

The final bound water distribution in the model is independent of the water migration scheme, due to the limited amount of initial water, but water migration schemes do influence the evolution of the water distribution in the mantle (Fig. 6d). Due to the limited amount of water that mantle material can absorb, the mantle is rapidly saturated by water released from the dehydrating cylinder. Therefore the faster the vertical migration of water, the faster the mantle hydrates (Fig. 6d). Due to the much higher water saturation values in the lithosphere, the effective water migration velocity in the overlying lithosphere is greatly reduced and differences in migration schemes are negligible there. Increasing the efficiency factor in the Darcy flow models (ϖ in Eq. 8) by an order of magnitude can locally increases the water velocity by an order of magnitude. However, this has a limited influence on the distribution of water as the average water velocity in the Darcy model stays close to 10 cm yr^{-1} (Fig. 6g).

To simulate the effect of water on viscosity in these linear viscous models, a linear decrease in the lithospheric and mantle viscosity of 2 orders of magnitude is used over

SED
5, 1771–1815, 2013

a water content of 0 to 4000 ppm. This is of the same order of magnitude as obtained by including 4000 ppm in the Hirth and Kohlstedt (2003) dislocation or diffusion creep flow law for wet olivine. Including the influence of water on mantle viscosity does not change the overall water distribution of the models (Fig. 6). It does however have a small effect on the mechanical evolution of the model (Fig. 7). The lower viscosity values of the hydrated mantle above the cylinder increase the mantle flow velocity in this region, which results in an increase in the sinking velocity of the cylinder. However this effect is limited as it corresponds to a difference in velocity of 0.1 $\mathrm{cm\,yr^{-1}}$. This is because hydration only occurs directly above the sinking cylinder. The sinking velocity of the cylinder is less sensitive to lowering the viscosity above the cylinder than it would be to changing the mantle viscosity below the cylinder.

3.3 Stokes model discussion

Our Stokes flow models of cylinder dehydration and mantle hydration show that different numerical water migration schemes do not result in large differences in the distribution of water in the mantle. This is due to the vertical flow induced by the sinking of the cylinder in the area of mantle hydration combined with migration schemes being vertical. Coupling of water migration to the mantle flow will therefore impact the vertical component of water velocities only and water migration paths stay vertical. The water migration velocities for our three migration schemes are within the same order of magnitude, resulting in a similar water distribution. However, changing the magnitude of the water migration velocity does initially increase the hydration rate of the mantle and the hydration front rises at different velocities (Fig. 6d). This is a transient phenomenon as the models converge after ca. 2.4 Myr. The low water absorption capability of the mantle material results in rapid effective water migration velocities in the mantle, confirming the results of Arcay et al. (2005). Models that simulate a decrease in mantle viscosity with water content show an increase in mantle velocities and a slightly faster sinking of the cylinder. Overall, our simple models of a sinking wet cylinder in a dry mantle seem to indicate that the exact numerical implementation of water migration might be

SED
5, 1771–1815, 2013

secondary to the first order effect that water could have on the system. We will test this in the next section with thermo-mechanical models that also include horizontal mantle (wedge) flow components.

Figure 5 shows a one element thick ring of hydrated mantle around the subducting cylinder, on the lateral and bottom sides. This is an artefact of the free water migration scheme. Once a particle dehydrates, undersaturated particles of the element are hydrated first. When the contact between cylinder and mantle lies within that element, mantle particles can absorb the released water resulting in the hydrated ring around the cylinder.

4 The effects of (de)hydration on subduction

4.1 Subduction model setup

We investigate the effects of slab dehydration, water migration, and mantle wedge hydration using a model of a 70 Myr old oceanic lithosphere subducting under a 40 Myr oceanic lithosphere. The model without water follows Quinquis et al. (2013) and has been tested with a number of different numerical codes.

The oceanic plates are composed of two layers: (1) a 7 or 8 km crustal layer for the overriding and subducting lithospheres, respectively, composed of Bulk Oceanic Crust (BOC) (Chemia et al., 2010), and (2) a 32 km thick Serpentinised Harzburgite (SHB) layer (Chemia et al., 2010). The rheological and thermal parameters are given in Tables 3 and 4. We assume that the upper 16 km of the oceanic plates are hydrated to a certain degree through fractures in the oceanic crust. The upper kilometre of BOC is fully hydrated, resulting in an initial water content of 2.68 wt.% H_2O. Few faults exceed 1 km depth, resulting in an undersaturation of the remaining BOC. The initial water content of the BOC below 1 km depth is set at 1.5 wt.% H_2O. Finally, between 7 (or 8) to 15 (or 16) kilometres depth, the overriding and subducting SHB are also undersaturated at an initial water content of 2 wt.% H_2O. These values follow Rüpke et al. (2004) and Faccenda et al. (2012).

The model domain is 3000 km wide and 670 km deep (Fig. 8) and has the highest horizontal and vertical Eulerian resolution at the trench (1 km per element). The total number of elements is 473 × 269 (horizontal × vertical) and 16 particles per element are initially used. Due to the variable grid resolution, this series of models requires injection and deletion of particles to maintain elemental particle density between 12 and 36. The particle deletion scheme helps keep the code memory requirements reasonable. To maintain the overall water content of the model, particles are injected dry, whereas bound or free water of a deleted particle is distributed evenly over all other particles of the element. Subduction is initialised by a "weak seed" located at the interplate boundary. The "weak seed" simulates a pre-existing shear zone in the oceanic lithosphere separating the overriding and subducting plates. It is 14 km thick (in the direction perpendicular to the dip angle), extends to a depth of 82 km, and has a 35° dip angle. The top mechanical boundary is a true free surface (both v_x and v_y are free), whereas the bottom and left boundaries of the model are free-slip. Balanced material in- and outflow is defined on the right boundary of the model domain (the boundary parallel component is again free). To avoid strong shearing at the transition between in- and outflow, a linear velocity gradient from in- to outflow is defined over a 20 km depth interval. The inflow velocity is 5 cm yr^{-1} over the thermal thickness of the 70 Myr old lithosphere. The outflow velocity is imposed from a depth of −130 km to the bottom of the model domain at −670 km.

The initial thermal conditions of the 40 Myr (from $x = 0$ to $x = -1500$ km) and 70 Myr (from $x = 1500$ to $x = 3000$ km) old oceanic lithospheres are determined from the plate cooling model (Turcotte and Schubert, 2002) for a surface temperature of 0 °C, a mantle temperature of 1300 °C at 82 and 110 km depth, respectively, and a thermal diffusivity of 10^{-6} m^2 s^{-1}. The initial step in temperatures at $x = 1500$ km is rapidly diffused. During model evolution, the surface temperature is held at 0 °C and the bottom temperature (at $y = -670$ km) at 1440 °C, while the lateral sides are insulated (zero heat flux). A high conductivity ($k = 183.33\,\mathrm{W\,m^{-1}\,K^{-1}}$) is defined for the mantle to enforce the mantle adiabat of $0.25\,^{\circ}\mathrm{C\,km^{-1}}$ (Pysklywec and Beaumont, 2004).

The subduction models are run using the 3 water migration schemes. Because vertical grid size varies (coarsening downwards from 1 to 7 km per element), water migration velocities are no longer constant in the elemental scheme and vary between 10 and $70\,\mathrm{cm\,yr^{-1}}$. However, the bulk of the dehydration processes occurs in the mantle wedge and there our model has a constant mesh resolution and therefore a constant water migration velocity of $10\,\mathrm{cm\,yr^{-1}}$. The elemental and Darcy flow schemes are also used to investigate the evolution of models with or without the effect of water content on viscosity (Eq. 4). The Darcy flow model uses an efficiency factor of 0.1 (Eq. 8). The vectorial migration scheme with imposed velocity is only calculated with water viscosity depending on water content. For this scheme two water velocities are investigated: $v_{\mathrm{f},y} = 5\,\mathrm{cm\,yr^{-1}}$ and $10\,\mathrm{cm\,yr^{-1}}$.

4.2 Subduction model results

Subduction is initiated at the weak seed by pushing the 70 Myr oceanic plate inwards, resulting in ca. 15 km trench migration until brittle failure helps localise deformation at the trench. The slab subducts at a fairly steep angle and with a more-or-less constant sinking velocity. The hydrated portion of the slab is limited to the top 16 km, and most of the slab is dry and therefore stiff. As we discuss below, the evolution of this stiff subducting slab is affected by (de)hydration processes but not in overwhelming degree.

Main dehydration occurs at two locations in the slab: at ca. 150 km depth where dehydration occurs at the phase transition of blueschists to eclogite, and 210 km depth where dehydration of chlorite occurs (Figs. 9 and 10). The mantle wedge is hydrated by these dehydration reactions. Hydrated mantle wedge material is entrained by the downwards flow above the subducting slab. This can bring bound water down to the transition zone. Figure 9 shows that the horizontal width of hydrated mantle above the slab decreases with depth. In the wedge, i.e, above 200 km depth, the mantle can be hydrated up to a distance of 100 km away from the surface of the slab. As the slab deepens, the distance of hydrated mantle from the slab surface decreases, from 50 km at ca. 200 km depth to less than 10 km at the slab tip (Fig. 9).

Due to inflow of hydrated oceanic lithosphere during model evolution, the OH_{rms} of the subducting slab increases as the model evolves (Fig. 11b). After 3 Myr, the OH_{rms} of the slab decreases slightly. This represents the onset of dehydration and is synchronous to the increase in OH_{rms} of the mantle (Fig. 11a).

The numerical water migration schemes cause small differences in the distribution of bound water in the mantle. The differences in mantle OH_{rms} between the three water migration schemes correspond to variations in the lateral distribution of hydrated mantle material (Figs. 9 and 11a). The effects on the distribution of free water are more substantial (Fig. 10). The distribution of free water for the elemental and Darcy schemes is similar, but the free water domain is somewhat broader in the Darcy models. This is caused by the horizontal component of the mantle flow that is added to the free water velocity. Larger variations occur in the free water distribution for the imposed migration velocity scheme and can result in locally large quantities of free water of up to 4 wt.% H_2O (Fig. 10). However, in our models, free water has no effect on rheology and therefore no influence on the dynamics of the system.

Introducing the effect of water content on viscosity does not have a strong impact on the large scale mechanical evolution of the model. This is because the evolution of the subducting slab is controlled by its stiffness. Due to the relatively little amount of water present in the slab (which is initially hydrated up to 16 km depth), dehydration processes will not greatly affect evolution of the already stiff slab. We do find that water weakening of viscosity increases flow in the mantle wedge and slightly reduces the curvature of the slab (Figs. 13 and 14). This could point to the slab-lifting effect of corner flow (Tovish et al., 1978). Corner flow is more pronounced in the models that have water-dependent viscosity as a large part of the mantle above the slab is hydrated and thus weakened, promoting stronger mantle flow.

SED
5, 1771–1815, 2013

4.3 Subduction model discussion

Our models show a similar slab dehydration evolution as Rüpke et al. (2004), Arcay et al. (2005) and Cagnioncle et al. (2007). This is because a similar method for determining the locations of dehydration reactions are used in these experiments. The depths at which dehydration reactions occur are slightly different between these studies because of differences in the thermal structure of the slab in the models.

We find that the overall dynamics of our subduction model is not strongly influenced by the viscosity decrease of mantle materials due to increase in water content. We suggest that this may be caused by the subducting slab being fairly stiff. Our slab is largely dry and the recent flow law of Hirth and Kohlstedt (2003) results in an average viscosity of ca. 5×10^{23} Pa s which is up to 5 orders of magnitude above the viscosity of the mantle. The evolution of this strong slab is not greatly influenced by dehydration processes. Our models do show an increase in the corner flow (Fig. 13) but not on the same scale as that observed in the models of Arcay et al. (2005). The slab in the models of Arcay et al. (2005) dips at a shallower angle, which could focus corner flow and cause a larger effect of water on the flow field.

The numerical implementation of water migration has a significant effect on the distribution of free water in the mantle wedge (Fig. 10). In our models, this effect is not visible in the overall evolution of the model because free water does not affect the rheology of the mantle materials. However, we could speculate that the distribution of free water in the mantle wedge could influence the dynamics of subduction by changing the pore pressure, thereby changing the stress, and the viscosity. Similarly, the pore pressure effect of free water could reduce plastic yield stress, further reducing effective viscosities in the slab and brittle parts of the mantle wedge. In our simplified models of water migration we did not include melts. Melts are sinks that are thought to absorb most of the excess free water. This would then decrease the potential effects of free water on pore pressures. Water also decreases the temperature at which melting can occur, encouraging melting, and because melts have a low viscosity this could impact

SED
5, 1771–1815, 2013

subduction dynamics. A logical next step would therefore be to include the effects of melts in our models of subduction with (de)hydration processes.

The decrease of viscosity with water content does influence the bound water distribution in the mantle close to the surface of the subducting slab (Fig. 13). Due to the limited water absorption capabilities of the mantle and the weak mantle wedge, the flow in the mantle wedge is increased causing a further increase in the area over which the mantle is hydrated and weak. This suggests that subduction and mantle wedge studies that investigate (de)hydration processes should preferably include the dynamic effects of water on viscosity and thus mantle flow during model evolution.

We assumed that the mantle material in our models can contain up to 2000 ppm water at upper mantle pressures and temperatures (Bercovici and Karato, 2003). We find that hydrated mantle material up to 2000 ppm is entrained by the flow caused by the subducting slab down to the bottom of the model domain (Figs. 9 and 12). This therefore supports the initial assumptions used in the studies of slab dehydration at the transition zone (i.e. between 670 and 410 km) of Richard et al. (2006, 2007). This also agrees with experimentally determined phase diagrams that suggest water could be present in the transition zone or deeper (Ohtani et al., 2004; Komabayashi et al., 2005). The amount of water reaching the transition zone could be greatly increased by including other chemical reactions in the mantle wedge, such as serpentinization (Iwamori, 1998). We show that including the weakening effect of water on viscosity increases the amount of water brought down to the bottom of the model domain (Fig. 13), because of the resulting stronger corner flow.

5 Conclusions

We have used a linear viscous Stokes flow model and a thermo-mechanical subduction model to investigate the effects of the numerical implementation of free water migration. We find that (de)hydration influences our models, but that the exact manner of water migration is not that important. This implies that studies of especially large-scale

SED
5, 1771–1815, 2013

dynamics may use a simple implementation of free water migration to capture the main effects of (de)hydration. We suggest an imposed velocity or simple Darcy flow water migration scheme. Elemental water migration (simply moving free water up one element per time step) is equally fine as long as grid resolution is constant and it is realised that grid size determines the water migration velocity.

We do find that the different water migration schemes influence the distribution of free water in subduction models. Elemental water migration results in a localised distribution of free water, while an imposed water migration velocity and Darcy flow result in a broader distribution of free water in the mantle wedge. This effect is caused by the free water being moved by the mantle flow in the latter migration schemes. Free water could effect pore pressure and thus material strength, but melting could decrease the amount of free water and the effect of free water on a subduction system therefore requires future study.

Including the effects of bound water content on viscosity does not strongly impact the overall evolution of the subducting slab as it is controlled by the slab stiffness. We do find that, the decrease in mantle viscosity with increasing water content as slab dehydration continues, causes a more vigorous corner flow. If we assume that the upper mantle contains an average of 2000 ppm water, this allows saturated hydrated mantle material to be transported down to the base of the upper mantle, supporting previous assumptions of hydrated material residing in the mantle transition zone.

Acknowledgements. We acknowledge financial support from the European Commission through Marie-Curie Research Training Network "c2c" (contract MRTN-CT-2006-035957). SULEC is developed jointly by Susanne Buiter and Susan Ellis. We warmly thank Zurab Chemia, Mark Caddick and James Connolly for help with Perple_X calculations and discussions on water behaviour, and Joya Tetreault for many numerical discussions.

SED
5, 1771–1815, 2013

References

Arcay, D., Tric, E., and Doin, M.-P.: Numerical simulations of subduction zones – effect of slab dehydration on the mantle wedge dynamics, Phys. Earth Planet. In., 149, 133–153, 2005. 1774, 1775, 1779, 1780, 1785, 1790, 1803

Bercovici, D. and Karato, S.-I.: Whole mantle convection and the transition-zone water filter, Nature, 425, 39–44, 2003. 1773, 1775, 1779, 1791

Billen, M. I.: Modeling the dynamics of subducting slabs, Annu. Rev. Earth Pl. Sc., 36, 325–356, doi:10.1146/annurev.earth.36.031207.124129, 2008. 1774

Billen, M. I. and Gurnis, M.: A low viscosity wedge in subduction zones, Earth Planet. Sc. Lett., 193, 227–236, 2001. 1774

Buiter, S. J. H. and Ellis, S. M.: Benchmarking a new ALE Finite-Element code, Geophys. Res. Abstracts, 14, EGU2012-7528, 2012. 1778

Caddick, M. J. and Thompson, A. B.: Quantifiying the tectono-metamorphic evolution of Pelitis rocks from a wide range of tectonic settings: mineral compositions in equilibrium, Contrib. Mineral. Petr., 156, 177–195, doi:10.1007/s00410-008-0280-6, 2008.

Cagnioncle, A.-M., Parmentier, E., and Elkins-Tanton, L.: Effect of solid flow above a subducting slab on water distribution and melting at convergent plate boundaries, J. Geophys. Res., 112, B09402, doi:10.1029/2007JB004934, 2007. 1775, 1790

Cheadle, M. J., Elliott, M. T., and McKenzie, D.: Percolation threshold and permeabiliy of crystallizing igneous rocks: the importance of textural equilibrium, Geology, 32, 757–760, doi:10.1130/G20495.1, 2004. 1773, 1775

Chemia, Z., Dolejš, D., and Steinle-Neumann, G.: Thermal effects of metamorphic reactions in a three component slab, Geophys. Res. Abstracts 12, EGU2010-5768, 2010. 1778, 1786, 1798, 1802

Connolly, J. A. D.: Computation of phase equilibria by linear programming: a tool for geodynamic modeling and its application to subduction zone decarbonation, Earth Planet. Sc. Lett., 236, 524–541, doi:10.1016/j.epsl.2005.04.033, 2005. 1773, 1774, 1778, 1779

de Capitani, C. and Brown, T. H.: The computation of chemical equilibrium in complex systems containing non-ideal solutions, Geochim. Cosmochim. Ac., 51, 2639–2652, 1987. 1774

England, P., Engdahl, R., and Thatcher, W.: Systematic variation in the depths of slabs beneath arc volcanoes, Geophys. J. Int., 156, 337–408, doi:10.1111/j.1365-246X.2003.02132.x, 2004. 1774

Faccenda, M., Burlini, L., Gerya, T. V., and Mainprice, D.: Fault-induced seismic anisotropy by hydration in subducting oceanic plates, Nature, 455, 1097–1100, doi:10.1038/nature07376, 2008. 1773, 1780

Faccenda, M., Gerya, T. V., Mancktelow, N. S., and Moresi, L.: Fluid flow during slab unbending and dehydration: implications for intermediate-depth seismicity, slab weakening and deep water recycling, Geochem. Geophy. Geosy., 13, Q01010, doi:10.1029/2011GC003860, 2012. 1787

Fujita, K. and Ogawa, M.: A preliminary numerical study on water-circulation in convecting mantle with magmatism and tectonic plates, Phys. Earth Planet. Int., 216, 1–11, doi:10.1016/j.pepi.2012.12.003, 2013. 1775

Gerya, T. V., Stöckhert, B., and Perchuk, A. L.: Exhumation of high pressure metamorphic rocks in a subduction channel: a numerical simulation, Tectonics, 21, 6-1–6-19, doi:10.1029/2002TC001406, 2002. 1774, 1775

Gerya, T. V., Connolly, J. A. D., and Yuen, D. A.: Why is terrestrial subduction one-sided?, Geology, 36, 43–46, doi:10.1130/G24060A.1, 2007. 1773, 1774

Gorczyk, W., Gerya, T. V., Connolly, J. A. D., and Yuen, D. A.: Growth and mixing dynamics of the mantle wedge plumes, Geology, 35, 587–590, 2007. 1774, 1775, 1780

Handin, J.: On the Coulomb-Mohr failure criterion, J. Geophys. Res., 74, 5343–5348, 1969. 1777

Handy, M., Hirth, G., and Bürgmann, R.: Continental fault structure and rheology from the frictional-to-viscous transition downward, in: Tectonic Faults: Agents of Change on a Dynamic Earth, edited by: Handy, M. R. et al., MIT Press, Cambridge, MA, 139–181, 2007. 1778

Hirschmann, M. M.: Water, melting, and the deep earth H_2O cycle, Annu. Rev. Earth Pl. Sc., 34, 629–653, doi:10.1146/annurev.earth.34.031405.125211, 2006. 1773

Hirth, G. and Kohlstedt, D.: Rheology of the upper mantle and the mantle wedge: a view from the experimentalists, in: Inside the Subduction Factory, edited by: Eiler, J., vol. 138 of Geophys. Monogr. Seer., AGU, Washington, D.C., 83–105, 2003. 1777, 1785, 1790, 1801

Holland, T. J. B. H. and Powell, R.: An internally consistent thermodynamic data set for phases of petrological interest, J. Metamorph. Geol., 16, 309–343, 1998. 1774

Hubbert, M. K. and Rubey, W. W.: Role of fluid pressure in mechanics of overthrust faulting: I. Mechanics of fluid-filed porous solids and its application to overthrust faulting, Geol. Soc. Am. Bull., 70, 115–166, 1959. 1778

Discussion Paper | Discussion Paper | Discussion Paper | Discussion Paper |

Iwamori, H.: Transportation of H_2O and melting in subduction zone, Earth Planet. Sc. Lett., 160, 65–80, 1998. 1773, 1774, 1775, 1779, 1791

Iwamori, H.: Seismic evidence for deep-water transportation in the mantle, Chem. Geol., 239, 182–198, 2007. 1774, 1775

Jaeger, J. C. and Cook, N. G. W.: Fundamentals of Rock Mechanics, Chapman and Hall, New York, 488 pp., 1976. 1777

Karato, S.-I. and Li, P.: Diffusion creep in perovskite and the linear rheology of the Earth's lower mantle, Science, 255, 1238–1240, 1992. 1777

Katz, R. F., Spiegelman, M., and Holtzman, B.: The dynamics of melt and shear localization in partially molten aggregates, Nature, 442, 676–679, doi:10.1038/nature05039, 2006. 1775, 1780

Kaus, B. J. P., Mühlhaus, H.-B., and May, D. A.: A stabilization algorithm for geodynamic numerical simulations with a free surface, Phys. Earth Planet. In., 181, 12–20, doi:10.1016/j.pepi.2010.04.007, 2010. 1778

Kerrick, D. M. and Connolly, J. A. D.: Metamorphic devolatilization of subducted oceanic metabasalts: implications for seismicity, arc magamtism and volatile recycling, Earth Planet. Sc. Lett., 189, 19–29, 2001. 1773

Komabayashi, T., Hirose, K., Funakoshi, K.-I., and Takafuji, N.: Stability of phase A in antigorite (serpentine) composition determined by in situ X-ray pressure observations, Phys. Earth Planet. In., 151, 276–289, 2005. 1774, 1791

Lemiale, V., Mühlhaus, H.-B., Moresi, L., and Stafford, J.: Shear banding analysis of plastic models formulated for incompressible viscous flows, Phys. Earth Planet. Int., 171, 177–186, doi:10.1016/j.pepi.2008.07.038, 2008. 1778

Ohtani, E., Litasov, K., Hosoya, T., Kubo, T., and Kondo, T.: Water transport into the deep mantle and formation of a hydrous transition zone, Phys. Earth Planet. In., 143–144, 255–269, doi:10.1016/j.pepi.2003.09.015, 2004. 1773, 1774, 1791

Peacock, S.: Thermal effects of metamorphic fluids in subduction zones, Geology, 15, 1057–1060, 1987. 1773

Powell, R., Holland, T. J. B. H., and Worley, B.: Calculating phase diagrams involving solid solutions via non-linear equations, with examples using THERMOCALC, J. Metamorph. Geol., 16, 577–588, 1998. 1774

SED
5, 1771–1815, 2013

Effects of water migration on subduction

M. E. T. Quinquis and S. J. H. Buiter

Pysklywec, R. N. and Beaumont, C.: Intraplate tectonics: feedback between radioactive thermal weakening and crustal deformation driven by mantle lithosphere instabilities, Earth Planet. Sc. Lett., 221, 275–292, 2004. 1783, 1788

Quinquis, M. E. T., Buiter, S. J. H., and Ellis, S.: The role of boundary conditions in numerical models of subduction zone dynamics, Tectonophysics, 497, 57–70, doi:10.1016/j.tecto.2010.11.001, 2011. 1778

Quinquis, M. E. T., Buiter, S. J. H., Tosi, N., Thieulot, C., Maierová, P., and Quinteros, J.: A numerical model setup for subduction: from linear viscous to thermo-mechanical rheologies, Geophys. Res. Abstracts, 15, EGU2013-7255-1, 2013. 1786

Ranalli, G.: Rheology of the Earth, 2nd edn., Chapman & Hall, London, UK, 392 pp., 1995. 1801

Regenauer-Lieb, K., Yuen, D. A., and Branlund, J. M.: The initiation of subduction: criticality by addition of water?, Science, 294, 578–580, doi:10.1126/science.1063891, 2001. 1774

Richard, G. C. and Bercovici, D.: Water-induced convection in the Earth's mantle transition zone, J. Geophys. Res., 114, B01205, doi:10.1029/2008JB005734, 2009. 1775

Richard, G. C. and Iwamori, H.: Stagnant slab, wet plumes and Cenozoic volcanism in East Asia, Phys. Earth Planet. In., 183, 280–287, doi:10.1016/j.pepi.2010.02.009, 2010. 1774, 1775

Richard, G. C., Bercovici, D., and Karato, S.-I.: Slab dehydration in the Earth's mantle transition zone, Earth Planet. Sc. Lett., 251, 156–167, doi:10.1016/j.epsl.2006.09.006, 2006. 1775, 1780, 1791

Richard, G. C., Monnereau, M., and Rabinowicz, M.: Slab dehydration and fluid migration at the base of the upper mantle: implications for deep earthquake mechanisms, Geophys. J. Int., 168, 1291–1304, doi:10.1111/j.1365-246X.2006.03244.x, 2007. 1775, 1791

Rüpke, L. H., Phipps Morgan, J., Hort, M., and Connolly, J. A. D.: Serpentine and the subduction zone water cycle, Earth Planet. Sc. Lett., 223, 17–34, doi:10.1016/j.epsl.2004.04.018, 2004. 1773, 1775, 1779, 1780, 1787, 1790

Schmeling, H., Babeyko, A. Y., Enns, A., Faccenna, C., Funiciello, F., Gerya, T. V., Golabek, G. J., Grigull, S., Schmalholz, S., and van Hunen, J.: A benchmark comparison of spontaneous subduction models – towards a free surface, Phys. Earth Planet. Int., 171, 198–223, doi:10.1016/j.pepi.2008.06.028, 2008. 1778

Schmidt, M. and Poli, S.: Experimentally based water budgets for dehydrating slabs and consequences for arc magma generation, Earth Planet. Sc. Lett., 163, 361–379, 1998. 1773, 1774, 1778, 1779, 1803

Sibson, R. H.: Fault rocks and fault mechanisms, J. Geol. Soc. London, 133, 191–213, 1977. 1778

Sibson, R. H., Moore, J. M., and Rankin, A. H.: Seismic pumping – a hydrothermal fluid transport mechanism, J. Geol. Soc. London, 131, 653–659, 1975. 1773

Staudigel, H.: Hydrothermal alteration processes in the Oceanic Crust, in: Treatise of Geochemistry, vol. 3, chap. 15, edited by: Holland, H. and Turekian, K., 511–537, 2003. 1773

Stern, R.: Subduction zones, Rev. Geophys., 40, 3-1–3-38, doi:10.1029/2001RG000108, 2002. 1773, 1774, 1775

Syracus, E. M. and Abers, G. A.: Global compilations of variations in slab depth beneath arc volcanoes and implications, Geochem. Geophy. Geosy., 7, Q05017, doi:10.1029/2005GC001045, 2006. 1773, 1774

Tingle, T., Green, H. W., Scholz, C. H., and Koczynski, T. A.: The rheology of faults triggered by the olivine-spinel transformation in Mg_2GeO_4 and its implications for the mechanism of deep-focus earthquakes, J. Struct. Geol., 15, 1249–1256, 1993. 1778

Tovish, A., Schubert. G., and Luyendyk, B. P.: Mantle flow pressure and the angle of subduction: non-newtonian corner flows, J. Geophys. Res., 83, 5892–5898, 1978. 1789

Turcotte, D. L. and Schubert, G.: Geodynamics, 2nd edn., Cambridge Univ. Press, 186 pp., 2002. 1782, 1787

Twiss, R. J. and Moores, E. M.: Structural Geology, W. H. Freeman and Company, New York, 532 pp., 1992. 1777

van den Berg, A. P., van Keken, P. E., and Yuen, D. A.: The effects of a composite non-Newtonian and Newtonian rheology on mantle convection, Geophys. J. Int., 115, 62–78, 1993. 1777

Wark, D. A., Williams, C. A., Watson, E. B., and Price, J. D.: Reassessment of pore shapes in microstructurally equilibrated rocks, with implications for permeability of the upper mantle., J. Geophys. Res., 108, B1, doi:10.1029/2001JB001575, 2003. 1773, 1775

White, S. H. and Knipe, R. J.: Transformation-and reaction-enhanced ductility in rocks, J. Geol. Soc. London, 135, 513–516, 1978. 1778

Table 1. Bulk compositions in % for the lithological oceanic lithosphere model (Chemia et al., 2010).

Oxides	BOC	SHB
SiO_2	47.32	41.023
TiO_2	0.63	0.075
Al_2O_3	16.11	1.114
FeO	7.21	7.66
MgO	9.27	42.298
CaO	12.17	1.029
Na_2O	1.65	–
H_2O	2.68	6.8
CO_2	2.95	–
Total	99.99	99.999

SED
5, 1771–1815, 2013

M. E. T. Quinquis and S. J. H. Buiter

Table 2. Input parameters for the linear viscous Stokes flow model. For all materials thermal expansivity $\alpha = 0$ and heat production $H = 0$.

Lithology	Parameter	Symbol	Unit	Value
Dry Lithosphere	Reference density	ρ_0	$\mathrm{kg\,m^{-3}}$	3200
	Viscosity	η	Pa s	10^{20}
	Thermal conductivity	k	$\mathrm{W\,m^{-1}\,K^{-1}}$	4.5
	Specific heat	C_p	$\mathrm{J\,kg^{-1}\,K^{-1}}$	750
Dry Mantle	Reference density	ρ_0	$\mathrm{kg\,m^{-3}}$	3200
	Viscosity	η	Pa s	10^{23}
	Thermal conductivity	k	$\mathrm{W\,m^{-1}\,K^{-1}}$	105
	Specific heat	C_p	$\mathrm{J\,kg^{-1}\,K^{-1}}$	1250
Hydrated Cylinder	Reference density	ρ_0	$\mathrm{kg\,m^{-3}}$	3250
	Viscosity	η	Pa s	10^{23}
	Thermal conductivity	k	$\mathrm{W\,m^{-1}\,K^{-1}}$	4.5
	Specific heat	C_p	$\mathrm{J\,kg^{-1}\,K^{-1}}$	1250

Table 3. Subduction model parameters. The viscosity ranges from a minimum of 10^{18} to a maximum of 10^{24} Pa s. Heat production $H = 0$.

Parameter	Symbol	Unit	Mantle	Sublithospheric mantle	Overriding plate BOC	Overriding plate SHB	Subducting plate BOC	Subducting plate SHB	Weak seed
Olivine rheology			Dry	Dry	Wet	Wet	Wet	Wet	Wet
Angle of friction[a]	ϕ		20°/10°	20°/10°	20°/10°	20°/10°	5°/2°	10°/5°	2°
Cohesion	C	MPa	20	20	15	15	5	15	5
Reference density	ρ_0	$kg\,m^{-3}$	3200	3200	3000	3250	3000	3250	3200
Reference temperature	T_0	°C	1300	1300	200	200	200	200	200
Conductivity	k	$W\,m^{-1}\,K^{-1}$	183.33	2.5	2.5	2.5	2.5	2.5	2.5
Heat capacity	C_p	$J\,kg^{-1}\,K^{-1}$	750	750	750	750	750	750	750
Thermal expansivity	α	$10^{-5}\,K^{-1}$	2.5	2.5	2.5	2.5	2.5	2.5	2.5
Initial water content	–	wt.% H_2O	0	0	1.5–2.68	2	1.5–2.68	2	2.68

[a] Angle of internal friction (ϕ) softens from first to second value over an effective strain interval of 0.5 to 1.5.

SED
5, 1771–1815, 2013

Effects of water migration on subduction

M. E. T. Quinquis and S. J. H. Buiter

Table 4. Flow law parameters from Hirth and Kohlstedt (2003).

Parameter	Unit	Dry Olivine Diffusion	Dry Olivine Dislocation	Wet Olivine Diffusion	Wet Olivine Dislocation
A[a]	$\mathrm{Pa}^{-n}\,\mathrm{m}^{p}\,\mathrm{s}^{-1}\,\mathrm{H}(10^6\mathrm{Si})^{-1}$	2.25×10^{-15}	6.514×10^{-16}	1.5×10^{-18}	5.3301×10^{-19}
n	–	1	3.5	1	3.5
Q	$\mathrm{kJ\,mol^{-1}}$	375	530	335	480
V	$10^{-6}\,\mathrm{m^3\,mol^{-1}}$	4	14	4	11
d	mm	5	–	5	–
p	–	3	–	3	–
C_{OH}	$\mathrm{H}(10^6\mathrm{Si})^{-1}$	–	–	1000	1000
r	–	–	–	1	1.2

[a] A is given for a general state of stress, and was converted from a uni-axial stress (Ranalli, 1995).

SED
5, 1771–1815, 2013

M. E. T. Quinquis and S. J. H. Buiter

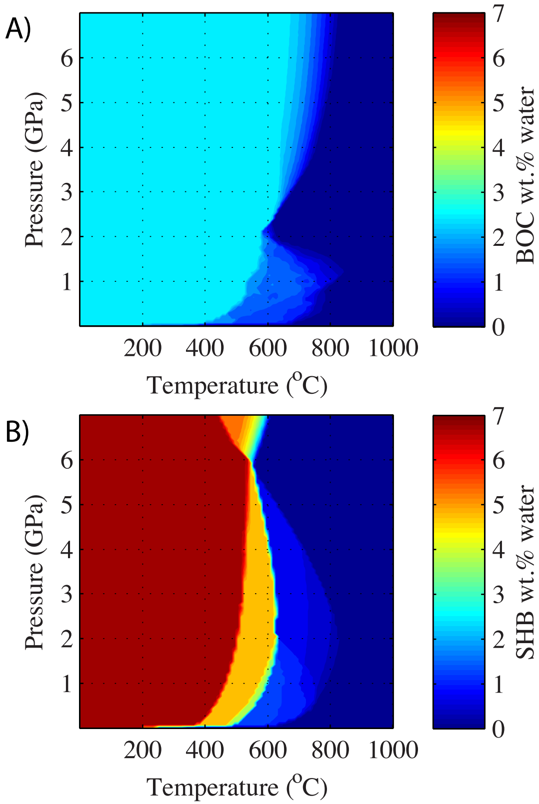

Fig. 1. Water content as a function of pressure and temperature calculated using Perple_X for **(A)** Bulk Oceanic Crust, and **(B)** Serpentinised Harzburgite lithologies (Chemia et al., 2010). Bulk compositions are in Table 1.

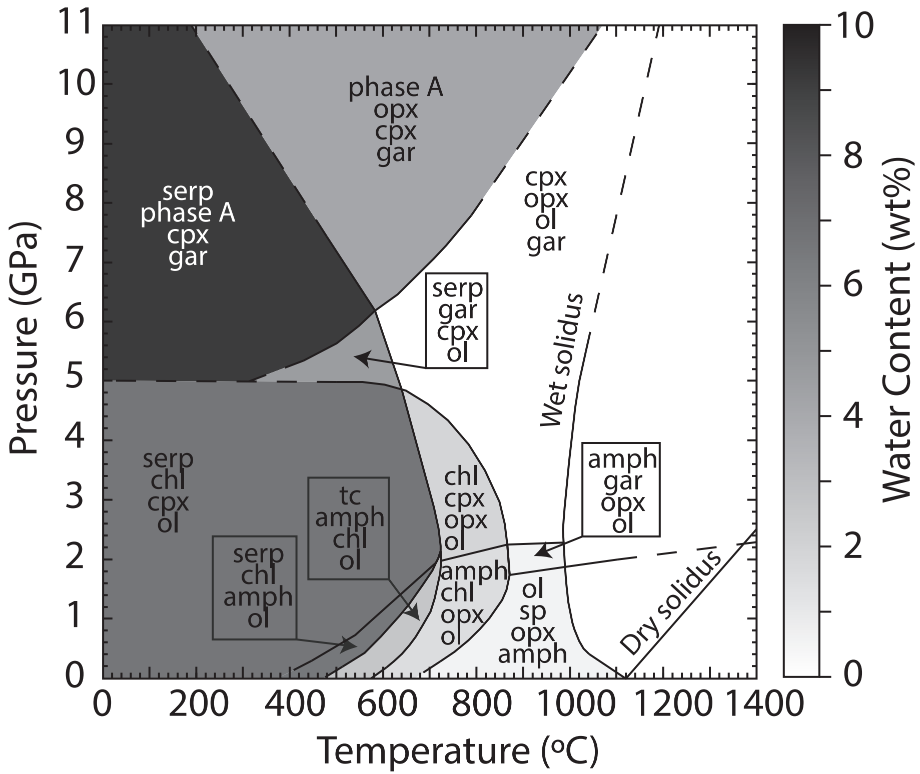

Fig. 2. Water content as a function of pressure and temperature for mantle material of pyrolitic composition, modified from Schmidt and Poli (1998). The solid lines are experimentally determined Clapeyron slopes (Schmidt and Poli, 1998), while the dotted lines have been extrapolated in a similar manner to Arcay et al. (2005). amph: amphibole; chl: chlorite; cpx: clinopyroxene; gar: garnet; opx: ortopyroxene; ol: olivine; serp: serpentine; sp: spinel; tc: talc.

SED
5, 1771–1815, 2013

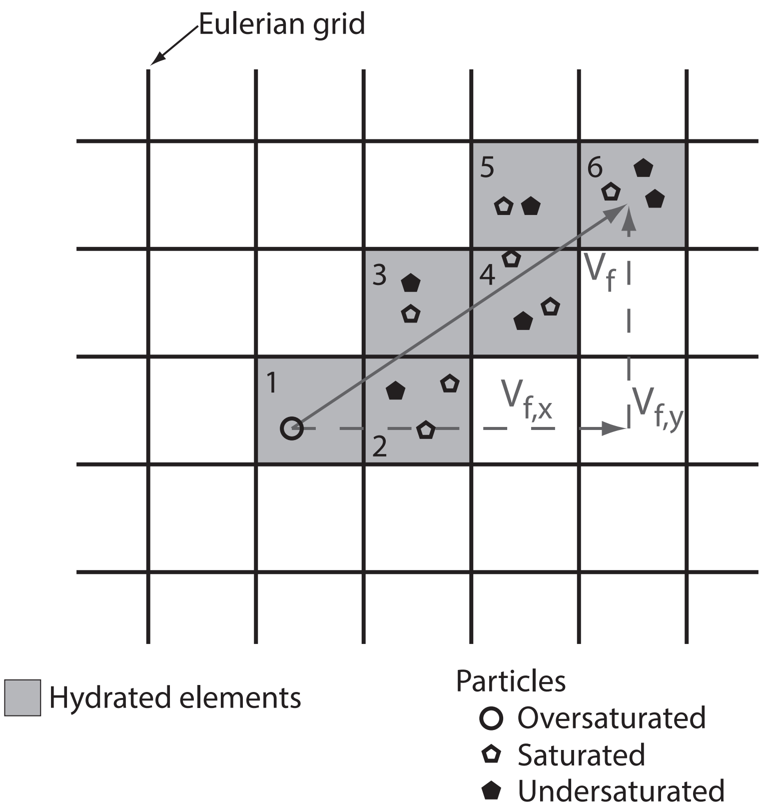

Fig. 3. Schematic migration of free water and it's distribution along a prescribed path for our velocity controlled water migration schemes 2 and 3 (see text for further explanation). V_f is water velocity.

SED
5, 1771–1815, 2013

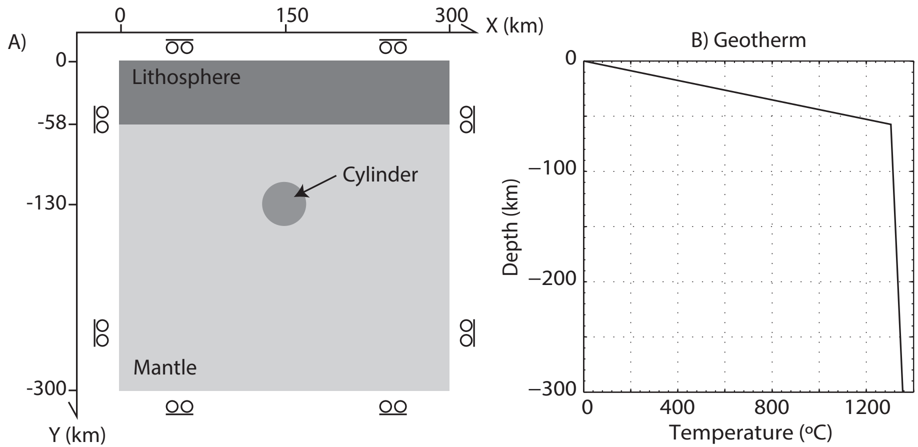

Fig. 4. (A) Model setup for a cold, hydrated cylinder sinking in a warm, dry mantle. All materials are linear viscous and their rheological parameters are given in Table 2. **(B)** Initial geotherm for model in **(A)**.

SED
5, 1771–1815, 2013

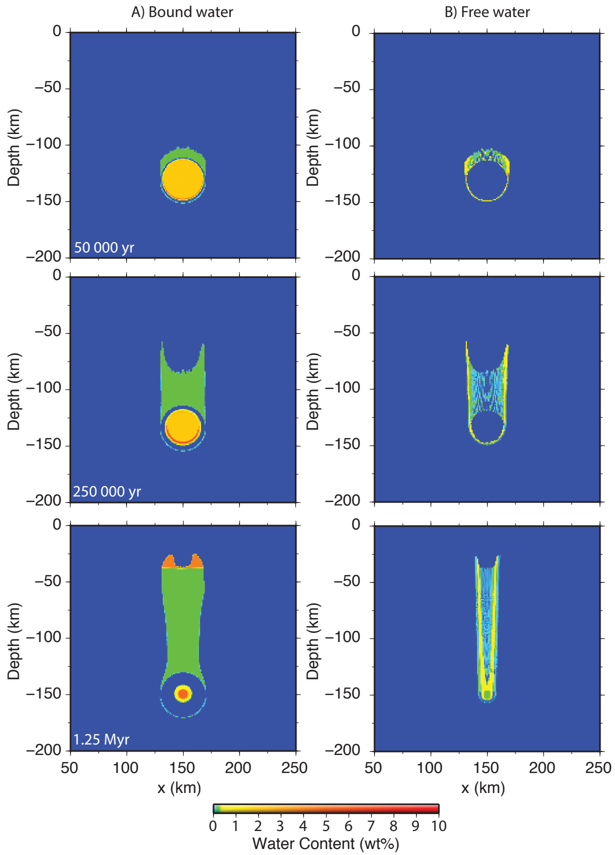

Fig. 5. Elemental water content for the Stokes flow models using the elemental water migration scheme (20 cm yr^{-1} for a grid resolution of 1 km × 1 km) showing **(A)** bound water, and **(B)** free water.

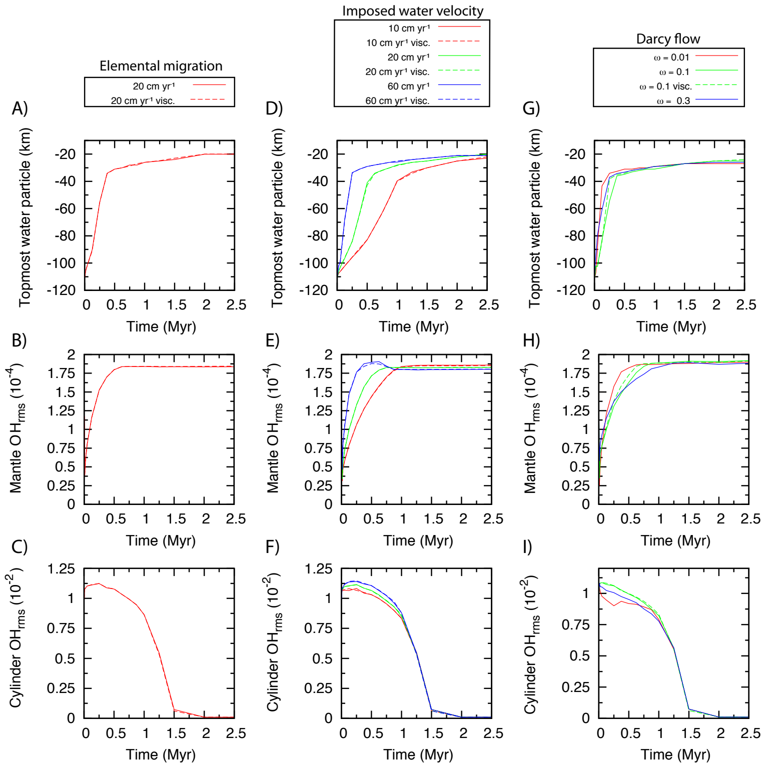

Fig. 6. Evolution with time of the depth of the top-most particle of hydrated material (top row), mantle OH_{rms} (middle row) and cylinder OH_{rms} (bottom row) for our Stokes models. The first column show results for the elemental migration scheme (water migration velocity of 20 cm yr^{-1}), the second for the vectorial migration scheme with different imposed velocities ($v_{f,y}$ = 10, 20 and 60 cm yr^{-1}) and the third for the vectorial migration scheme in which the water migration velocity is calculated using the Darcy law with efficiency factor ω = 0.01, 0.1 or 0.3 (Eq. 8). Models labelled "visc" have a decrease in viscosity with increasing water content.

SED
5, 1771–1815, 2013

M. E. T. Quinquis and S. J. H. Buiter

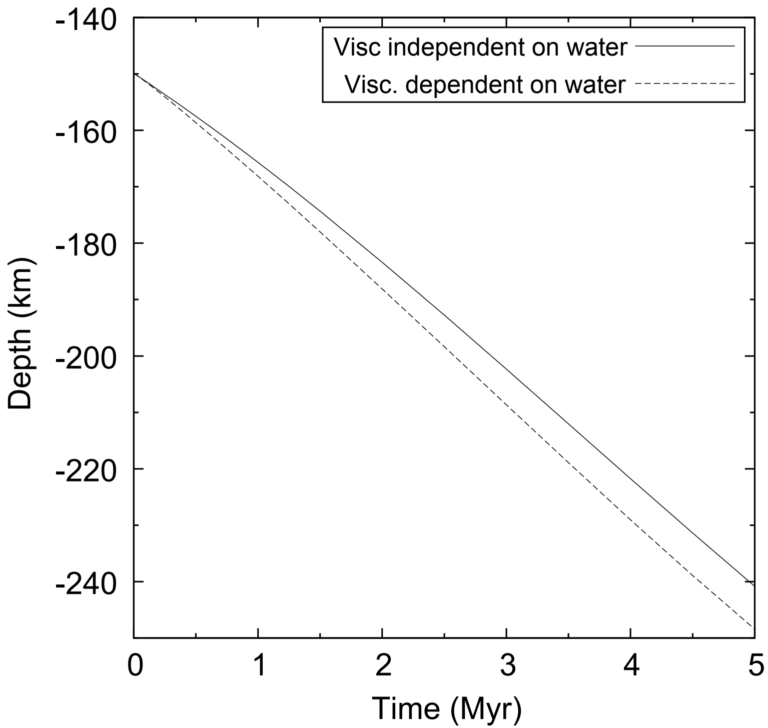

Fig. 7. Depth of the bottom of the subducting cylinder versus time for Stokes flow models with or without including the effects of water on viscosity. This figure is for models with an elemental water migration scheme (Fig. 6a–c).

SED
5, 1771–1815, 2013

Effects of water migration on subduction

M. E. T. Quinquis and S. J. H. Buiter

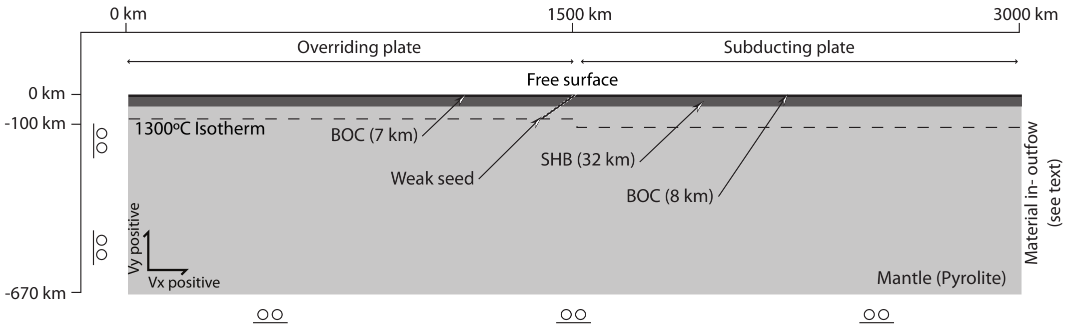

Fig. 8. Model setup for subduction of a 70 Myr old oceanic plate under a 40 Myr old oceanic plate. The top boundary is free. The bottom and left boundary are free-slip, while the right boundary condition includes material in- and outflow. SHB: Serpentinised Harzburgite, and BOC: Bulk Oceanic Crust.

SED
5, 1771–1815, 2013

M. E. T. Quinquis and S. J. H. Buiter

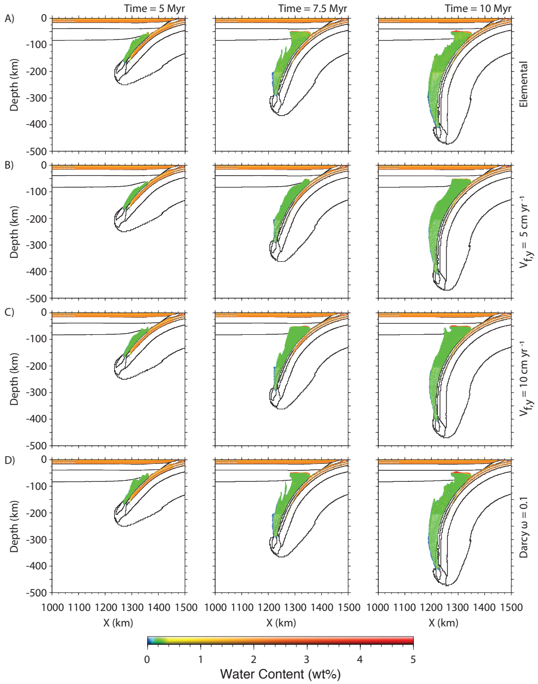

Fig. 9. Bound water distribution for subduction models after 5, 7.5 and 10 Myr for the following free water migration schemes: **(A)** elemental water migration (velocity $v_{f,y}$ increases from $10\,\mathrm{cm\,yr^{-1}}$ just below the lithosphere to $70\,\mathrm{cm\,yr^{-1}}$ at the base of the model where the grid is coarsest); **(B)** imposed vertical velocity $v_{f,y} = 5\,\mathrm{cm\,yr^{-1}}$; **(C)** imposed vertical velocity $v_{f,y} = 10\,\mathrm{cm\,yr^{-1}}$ and **(D)** Darcy velocity with efficiency factor $\varpi = 0.1$. Bound water moves with material flow. Viscosity of all materials changes with water content following the flow law of Eq. (4).

SED
5, 1771–1815, 2013

Effects of water migration on subduction

M. E. T. Quinquis and S. J. H. Buiter

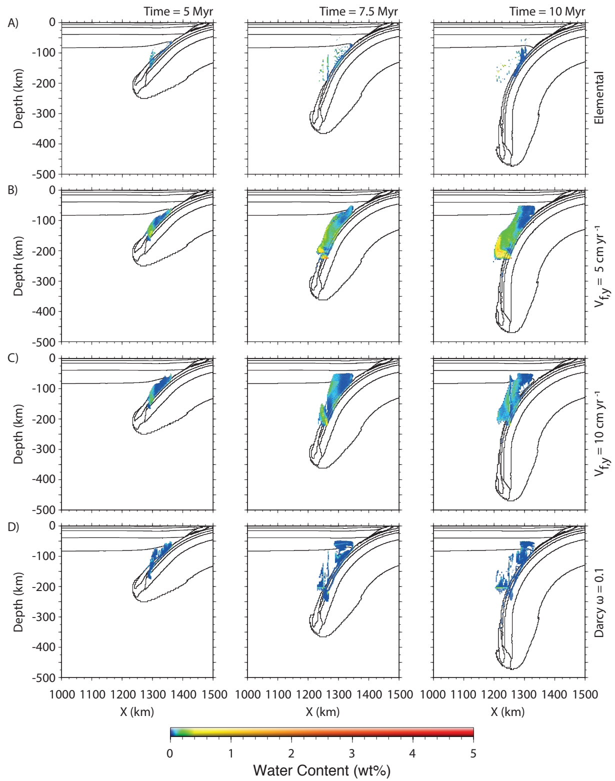

Fig. 10. Free water distribution for subduction models after 5, 7.5 and 10 Myr for the following water migration schemes: **(A)** elemental water migration (velocity $v_{f,y}$ varies between 10 and 70 $cm\,yr^{-1}$); **(B)** imposed vertical velocity $v_{f,y} = 5$ $cm\,yr^{-1}$; **(C)** imposed vertical velocity $v_{f,y} = 10$ $cm\,yr^{-1}$ and **(D)** Darcy velocity with efficiency factor $\omega = 0.1$. Viscosity of all materials changes with water content following flow law of Eq. (4).

SED
5, 1771–1815, 2013

Effects of water migration on subduction

M. E. T. Quinquis and S. J. H. Buiter

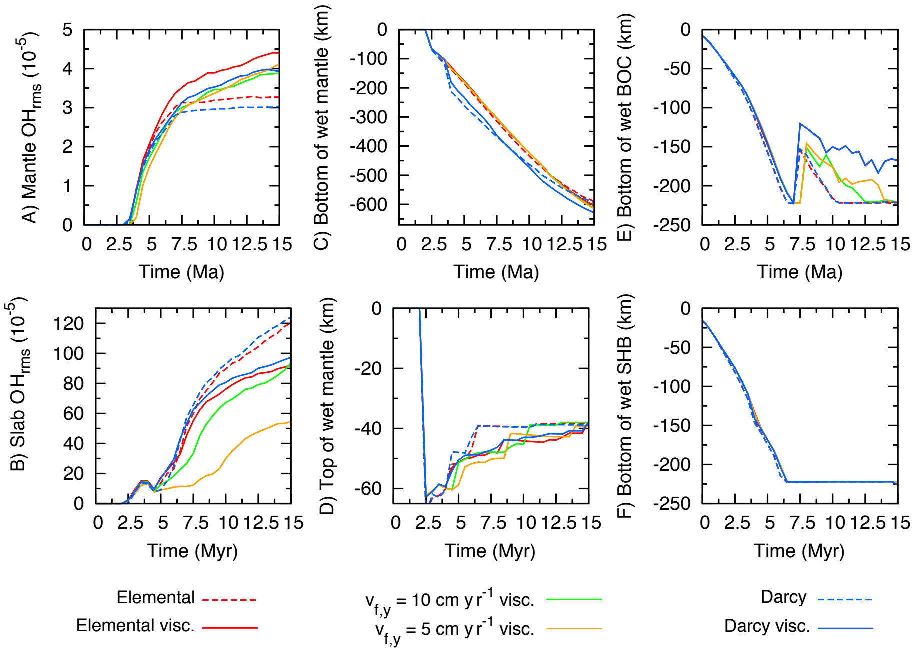

Fig. 11. Evolution of: **(A)** mantle OH$_{rms}$; **(B)** slab OH$_{rms}$; **(C)** depth of the lowermost particle of hydrated mantle; **(D)** depth of the topmost particle of hydrated mantle; **(E)** depth of the lowermost particle of hydrated BOC, and **(F)** depth of the lowermost particle of hydrated SHB for the subduction models. "visc" indicates models that have a decrease in viscosity with increasing water content.

SED
5, 1771–1815, 2013

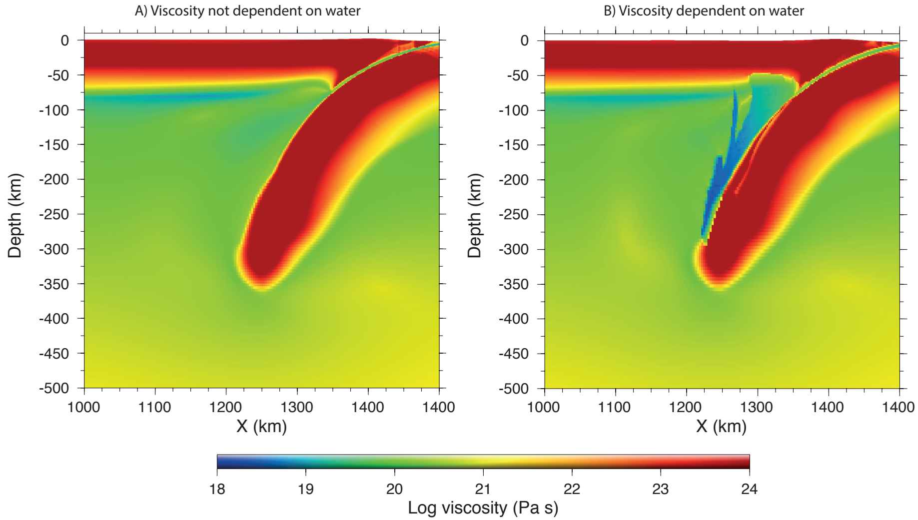

Fig. 12. Viscosity field for models including the Darcy water migration scheme with $\varpi = 0.1$ after 7.5 Myr for: **(A)** water content and viscosity not coupled, and **(B)** water content and viscosity coupled.

SED
5, 1771–1815, 2013

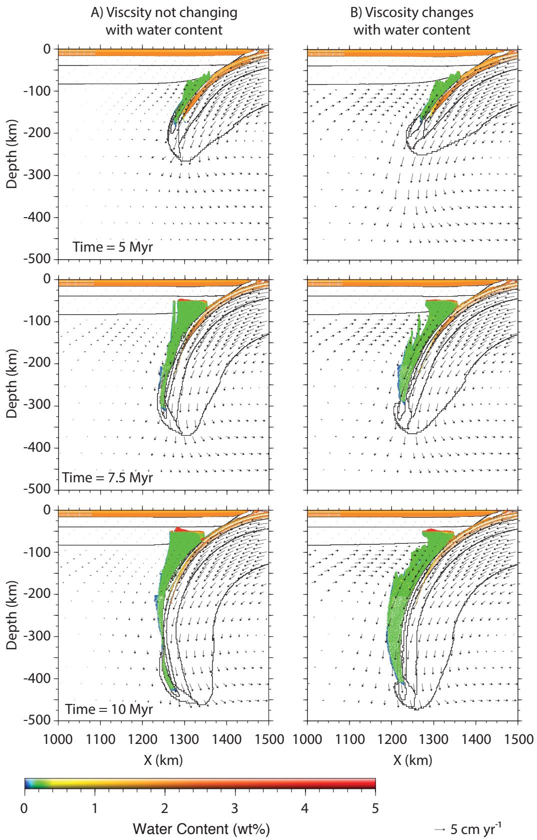

Fig. 13. Bound water distribution for subduction models using the Darcy water migration scheme (with efficiency factor $\varpi = 0.1$) at 5, 7.5 and 10 Myr. **(A)** Water content does not change viscosity; **(B)** water content is coupled to the viscosity (following flow law Eq. 4).

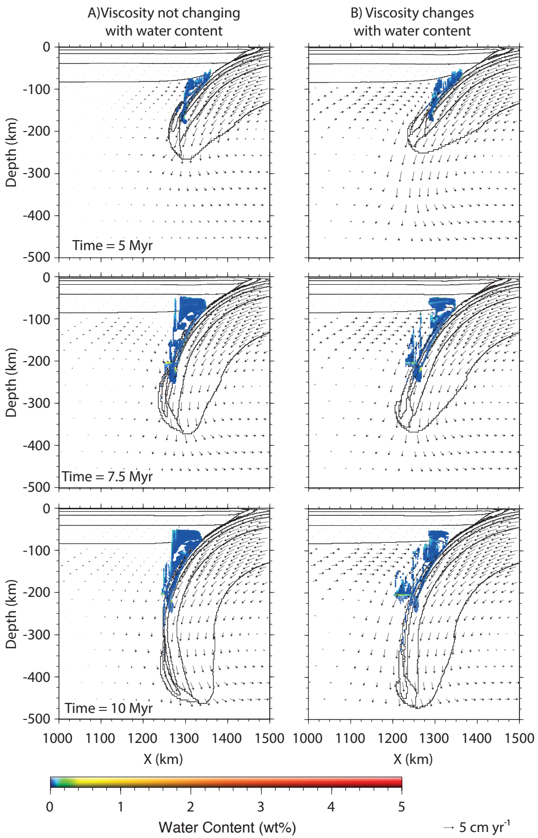

Fig. 14. Free water distribution for subduction models using the Darcy water migration scheme (with $\varpi = 0.1$) at 5, 7.5 and 10 Myr. **(A)** Water content does not change viscosity; **(B)** water content is coupled to the viscosity (following flow law Eq. 4).

SED
5, 1771–1815, 2013

Effects of water migration on subduction

M. E. T. Quinquis and S. J. H. Buiter